CrystEngComm

Accepted Manuscript

ROYAL SOCIETY OF CHEMISTRY

www.rsc.org/crystengcomm

Journal Name

ARTICLE

Electrochemical energy storage in Mn_2O_3 porous nanobars derived from morphology-conserved transformation of benzenetricarboxylate-bridged metal-organic framework

Received 00th January 20xx,
Accepted 00th January 20xx

DOI: 10.1039/x0xx00000x

www.rsc.org/

Sandipan Maiti, Atin Pramanik and Sourindra Mahanty*

Tailoring the morphology of mesoporous nanostructures toward performance enhancement plays a key role for developing efficient energy storage devices. Herein, we report formation of well crystallized Mn_2O_3 mesoporous nanobars through a simple *exo*-templeting of manganese 1,3,5-benzenetricarboxylate metal-organic framework (Mn-BTC MOF) by thermal treatment whereby the general morphology of the parent MOF is conserved, but with more voids and spaces. Parent Mn-BTC MOF was synthesized by solvothermal reaction of trimesic acid with manganese nitrate in alcoholic solution. The MOF-derived Mn_2O_3 was characterized by XRD, field-emission SEM, high-resolution TEM, and N_2 adsorption/desorption isotherm measurements. When examined as an anode material for lithium-ion battery in the potential windows of 0.01-3.0 V and 0.01-2.0 V, high reversible specific capacities of 849 and 778 mAh g^{-1} were obtained. It is found that the electrochemical processes are more reversible when cycled in the 2 V window. A steady capacity of ~410 mAh g^{-1} was observed after 300 continuous cycles at ~C/5.5 exhibiting good cycling stability in the 2 V window. When tested as a pseudocapacitor electrode in three-electrode configuration, specific capacitance of 250 F g^{-1} at 0.2 A g^{-1} could be achieved. Further, to demonstrate the practical applicability, two-electrode asymmetric supercapacitor pouch cells were assembled with Mn_2O_3 as the positive electrode and commercial activated carbon as the negative electrode which showed an ultrahigh energy density of 147.4 Wh kg^{-1} at a power density of 1004 W kg^{-1}. The present work shows the potential of MOF derived route for obtaining metal oxides with desired nano-architecture for electrochemical applications with high performance.

Introduction

In recent years, nanostructured metal oxides, especially transition metal oxides (TMO) have emerged as the most promising electrode materials for electrochemical energy storage.[1-6] In particular, considerable efforts are directed to develop TMOs as: (i) anode for lithium-ion battery (LIB) due to their high theoretic specific capacity originated from a novel conversion mechanism as demonstrated by Tarascon et al.[1] and (ii) pseudocapacitive electrode in supercapacitors due to their ability to yield much higher energy density (20-50 Wh kg^{-1}) than conventional carbon based materials (10-20 Wh kg^{-1}).[7,8] In order to exploit the full potential of transition metal oxides, synthesis of porous nanostructures with controlled nano-architecture and surface morphology is extremely important for achieving the desired application specific physico-chemical properties.[9,10] The ultimate electrochemical performance is strongly influenced by a combination of several parameters such as crystallinity, effective surface area, interconnected pores with controlled size and distribution, surface energy, chemical reactivity etc. Also, electrode fabrication engineering such as using strain-released hybrid multilayer anodes have led to significant enhancement in the field of LIB.[11-13] During the last decade, considerable work has been focused for synthesizing various forms of nanostructured porous transition metal oxides.[14] However, these efforts are mostly concentrated on wet chemical routes and despite the advancements made, and challenges still remain with respect to tailoring the morphology in an easily scalable controlled way with high degree of reproducibility. In this respect, metal organic frameworks (MOF), which are porous coordination polymers, offer the possibility of creating designer nanostructures by varying the nodal metal ions and the multi nodal organic linkers.[15,16] MOFs can be easily converted into metal oxides by calcination with creation of a large number of voids and spaces. A high surface area and a suitable pore size would allow maximum amount of the active sites to be exposed to the electrolyte, the condition most favorable for lithium-ion battery or supercapacitor applications. Recognizing

Fuel Cell & Battery Division, CSIR-Central Glass & Ceramic Research Institute, Kolkata 700032 and CSIR-Network Institutes for Solar Energy (NISE), India.
Email: mahanty@cgcri.res.in; s_mahanty@hotmail.com
Tel: +91-33-2322 3495 Fax: +91-33-2473 0957.
†Electronic Supplementary Information (ESI) available: XRD, TGA of Mn-BTC MOF and EDS of Mn_2O_3, XRD, FESEM of cycled electrode, additional electrochemical characterization.
See DOI: 10.1039/x0xx00000x

the opportunity, the field of MOF derived metal oxide is growing at a fast pace in recent years and several excellent reviews are available.[17-19] In this work, we have synthesized Mn_2O_3 porous nanostructures through calcination of Mn-BTC MOF and investigated the electrochemical properties both as LIB and supercapacitor electrodes. Though Mn_2O_3 possesses a relatively lower electronic conductivity compared to other forms of manganese oxide, the rationale behind selection of Mn_2O_3 being its high theoretical capacity of 1018 mAh g^{-1} as LIB anode (between 0-3 V) due to two redox processes occurring at ~1.3 V ($Mn^{o} \leftrightarrow Mn^{2+}$) and ~2.2 V ($Mn^{2+} \leftrightarrow Mn^{3+}$).[20] As most of the reversible capacity of Mn_2O_3 is generated by the first process (i.e., conversion reaction involving Mn and Li_2O), this offers us an opportunity to develop an anode with a relatively lower operating voltage vs. Li/Li^{+} (< 2 V). Additionally, Mn_2O_3 also has a high theoretical capacitance of 611 F g^{-1} as electrochemical pseudocapacitor.

There are several reports on Mn_2O_3 porous structures synthesized by wet chemical route,[21-33] where improved electrochemical performance with high capacity, good cycling stability, and rate capability could be obtained though in some cases the capacity retention upon cycling is poor.[34,35] Qiu et al.[36] have hydrothermally synthesized oval-shaped hierarchical structures and achieved a specific capacity of ~380 mAh g^{-1} after 150 cycles for straw-sheaf shaped Mn_2O_3. On the other hand, hollow rod-like Mn_2O_3, synthesized from bacterial templates showed a specific capacity of ~300 mAh g^{-1}.[37] Deng et al.[24] have reported a maximum specific capacity of 796 mAh g^{-1} at a current density of 100 mA g^{-1}, whereas, Dai et al.[25] showed a specific capacitance ~900 mAh g^{-1} at a relatively low current density 50 mA g^{-1} in the same potential window. Pal et al.[38] have observed that among different shapes, hollow spheres can yield a better capacity (478 $mAhg^{-1}$) with 38% retention after 30 cycles due its high accessible surface area and inner hollow architecture. Similarly, Li et al.[39] have shown that Cu-doped hollow spherical Mn_2O_3 exhibited a specific capacity of 642 mAh g^{-1} after 100 cycles at a current density of 100 mA g^{-1}. However, Lin et al.[27] have reported a capacity of ~750 mAh g^{-1} at 200 mAg^{-1} using triple-shelled Mn_2O_3 hollow nanocubes. A very high capacity (1442 mAh g^{-1} at 800 mA g^{-1}), exceeding the theoretical capacity, has recently been reported by Liu et al.[33] Very recently, Mn_2O_3 nanocrystallites with a porous structure obtained from calcination of $[Mn(Br_4\text{-bdc})(4\text{-}4'\text{-bpy})(H_2O)_2]_n$ (Br_4-bdc = tetrabromo terephthalate and 4-4'-bpy = 4-4'-bipyridine) shows an exceptionally high rate capability (705 mAh g^{-1} at 1 Ag^{-1}) studied in the potential window extended to 3.0 V.[32] These excellent studies highlight the importance of developing designer porous structure for enhancement of electrochemical performance. By changing the organic linkers, different manganese based MOFs could be obtained which would produce Mn_2O_3 with a different morphology.

In all the studies so far, the potential window was extended (up to 3.0 V) to accommodate the contribution from the additional redox process, $Mn^{2+} \leftrightarrow Mn^{3+}$, generating extra capacity. From the viewpoint of practical suitability, a potential window up to 2.0 V (utilizing only the $Mn^{o} \leftrightarrow Mn^{2+}$ redox process) would be more appropriate for an anode.

Mn_2O_3 is also being considered as a promising pseudocapacitor electrode due its pronounced electrochemical redox activity via Mn^{3+} to Mn^{4+} transition giving rise to a theoretical capacity of 611 F g^{-1} (one electron transfer process). Accordingly, several studies have been devoted for developing Mn_2O_3 or Mn_2O_3 based composites as pseudocapacitor in three-electrode cells,[40-47] or in two-electrode symmetric/asymmetric cells.[41,45,47] Nathan et al.[40] have found a psedocapacitance of 100 F g^{-1} from spherical nanoparticles of cubic Mn_2O_3 in 6 M KOH. Chen et al.[42] have observed a specific capacitance value of 202 F g^{-1} in 1 M Na_2SO_4 for α-Mn_2O_3 having different morphologies including spheres and polyhedrons. On the other hand, Li et al.[47] have demonstrated the specific capacitance values of 191 F g^{-1} and 53 F g^{-1} in 0.5 M Na_2SO_4 respectively in three and two electrode configuration using porous Mn_2O_3 nano-cubes. A specific capacitance of 306 F g^{-1} has been achieved by using Mn_2O_3 nanorod structure produced by the pulse reverse potential method.[43]

In order to improve the capacitance further, carbon based Mn_2O_3 composite have also been investigated. In neutral electrolyte, Park[46] has reported a pseudocapacitance value of 300 Fg^{-1} at a current density of 50 mA g^{-1} in 1.0 M Na_2SO_4 using carboxylated-graphene-Mn_2O_3 as the working electrode. On the other hand, Zhang et al.[44] have observed a pseudocapacitance value of 370 F g^{-1} at 100 mA g^{-1} in 1.0 M Na_2SO_4 in three electrode configuration from 3D graphene/CNTs/Mn_2O_3. In alkaline electrolyte (1 M NaOH), a pseucapacitance of 425 F g^{-1} at 5 mV s^{-1} has been obtained from rGO/Mn_2O_3/Mn_3O_4 in three electrode configuration and asymmetric supercapacitance of 133 F g^{-1} at 0.2 A g^{-1} has been obtained from rGO/Mn_2O_3/Mn_3O_4//graphene in two electrode configuration.[45] From the above literature survey, it can be seen that the specific capacitance of Mn_2O_3 nanostructures, synthesized by wet chemical routes, lies in the range 100-300 F g^{-1} in the pristine form and in the range 300-425 F g^{-1} in the composite form. So far, pseducapacitive property of Mn_2O_3, derived through MOF route has not been investigated.

Herein, we report synthesis of nanostructured Mn_2O_3 with controlled porous structure by MOF exo-templeting method where the morphology of the parent Mn-BTC MOF (BTC = 1,3,5-benzene-tricarboxylate) is retained but with a large proportion of voids and spaces. The electrochemical properties as 2 V LIB anode and as pseudocapacitor in three and two electrode configuration have been evaluated without forming any composite to investigate the effect of morphological features in isolation.

Experimental

Synthesis

The following chemicals were used for the synthesis of Mn-BTC and Mn_2O_3 thereof: manganese nitrate $Mn(NO_3)_2.4H_20$ (98+%, Acros Organics, USA), trimesic acid (H_3BTC) (~95%, Merck, Germany) and ethyl alcohol (C_2H_5OH) (Merck, Germany).

Mn-BTC metal-organic framework was synthesized by following a simple solvothermal process similar to the one as described in our previous work.[48] Briefly, two separate alcoholic solutions were prepared by dissolving (i) 7.5 mmol of $Mn(NO_3)_2.4H_2O$ in 50 ml of C_2H_5OH (solution-A) and (ii) 4.16 mmol of trimesic acid (H_3BTC) in 30 ml of C_2H_5OH (solution-B). Solution-B was added slowly to solution-A under constant stirring till a clear solution is obtained. The mixture was transferred to an autoclave and the reaction was allowed to continue for 4 days at 160°C under autogenously developed pressure. A light brown powder, thus obtained, was collected by centrifugation. After repeated washing by ethanol, the synthesized Mn-BTC powder was dried at 60°C for 12 h in an air oven.

Mn_2O_3 was synthesized via calcination of Mn-BTC MOF at 650°C for 3 h. The temperature of the furnace was raised at a rate of 2°C per min. The resulting powder was dark brown in colour. A schematic representation of the synthesis mechanism of Mn-BTC and Mn_2O_3 thereof is given in Scheme-1.

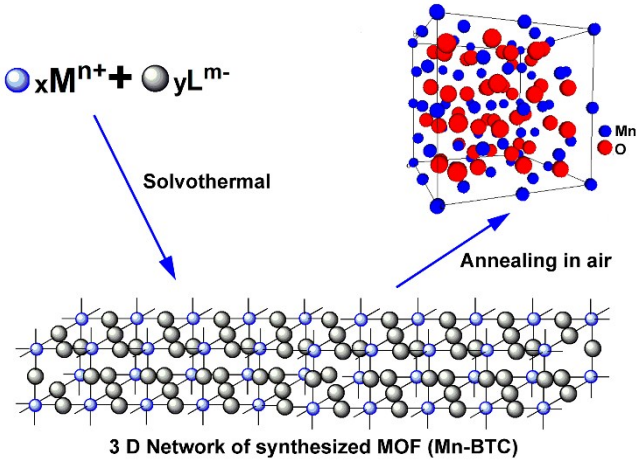

Scheme-1 Schematic representation for the synthesis of MOF derived Mn_2O_3

Activated carbon powder (carbon content >95%, ash content <0.07%), purchased from MTI Corporation, USA, was used for fabricating the negative electrode for asymmetric supercapacitor.

Material characterization

Phase purity and crystallinity were examined by powder x-ray diffraction (XRD), recorded in the 2Θ range 20°-80° at a scanning rate of 2° min^{-1} by a X-ray diffractometer (Philips X'Pert, the Netherlands) with a Cu-K_α radiation at 40 kV and 40 mA. Morphology and microstructural features were inspected by a ZEISS Supra 35 (Germany) field emission scanning electron microscope (FESEM). A transmission electron microscope (TEM), Tecnai G^2 30ST (FEI), operating at 300 kV was used to obtain the high resolution TEM images (HRTEM), selected area electron diffraction (SAED) pattern and energy-dispersive X-ray spectrum (EDS). Thermogravimetric analysis (TGA) was performed in air at a heating rate of 10°C min^{-1} using a Simultaneous Thermal Analyser (STA449F, Netzsch, Germany). Nitrogen gas adsorption-desorption measurements were carried out at 77.3 K using a Quantachrome (USA) Autosorb surface analyzer.

Electrochemical characterization

The electrochemical properties as LIB anode were evaluated in 2032 type coin cells vs Li/Li^+. First, a slurry was made by intimately mixing Mn_2O_3, Super-P carbon (conducting agent) and polyvinylidene fluoride (PVDF, binder) in a weight ratio of 70:20:10 in n-methyl pyrrolidinone (NMP, solvent). Then, the slurry was coated onto a copper foil of thickness 15 mm (current collector). After drying at 110°C for 5 h in a vacuum oven, circular disks were cut and used as working electrode. The area of the electrode was 1.76 cm^2 with typical active mass loading of ~2.0 mg cm^{-2}. For assembling LIB coin cells, Li metal served as the counter electrode as well as the reference electrode, Celgard 2300 as the separator and 1.0 M $LiPF_6$ in EC: DMC (1:2 vol:vol) as the electrolyte. Fabrication of coin cells was done inside an argon-filled glove box (M'BRAUN, Germany) where the moisture and oxygen levels were kept at <0.5 ppm. A potentiostat-galvanostat (PGSTAT30, Autolab, the Netherlands) was used for conducting cyclic voltammetry (CV) tests in the potential windows of 0.01-2.0 V and 0.01-3.0 V at a scanning rate of 0.1 mV s^{-1}. An automatic battery tester (BT2000, Arbin, USA) was used for galvanostatic charge-discharge (GCD) measurements in the same potential windows using a current density of 126 mA g^{-1} (C/5.5) for the initial formation cycle and at different current densities ranging from 251-1257 mA g^{-1} (C/2.7-1.9C) for subsequent cycles (0.01-2.0 V). For each cycle, charging and discharging were carried out at the same current density. Electrochemical impedance spectra (EIS) were recorded on a galvanostat-potentiostat (PGSTAT302N, Autolab, the Netherlands) in the frequency range of 10 mHz to 1 MHz with an AC amplitude of 5 mV.

The electrochemical properties as supercapacitor electrode were evaluated both in three-electrode beaker cells and two-electrode coin cells. For preparation of Mn_2O_3 electrode, the same slurry (as prepared above) was casted on nickel foil of size 2 cm x 2 cm (thickness ~ 0.2 mm) and dried at 110 °C for 5 h in a vacuum oven. The typical mass loading of Mn_2O_3 on Ni foil was ~1.0 mg cm^{-2}. Activated carbon (AC) electrodes were prepared from a slurry of AC and PVDF in a weight ratio of 90:10 in NMP following the same procedure of casting and drying. In three-electrode configuration, a platinum mesh (2

cm x 2 cm) was used as the counter electrode and Ag/AgCl (3 M KCl) as the reference electrode. Two-electrode asymmetric pouch cells were assembled with Mn_2O_3 electrode as the positive electrode and activated carbon (AC) as the negative electrode. The electrolyte used was 3 M KOH solution in all cases. All electrochemical measurements were carried out by using a galvanostat-potentiostat (PGSTAT302N, Autolab, the Netherlands). CVs were measured at various scan rates ranging from 2 mV s^{-1} to 100 mV s^{-1} in different potential windows of −1 to 0 V (Pt//AC), 0 to 0.45 V (Pt//Mn_2O_3) and 0 to 1.4 V (AC//Mn_2O_3). GCD measurements were carried out at current densities of 0.2-30.0 A g^{-1} in the potential windows 0.0-0.38 V (Pt//Mn_2O_3) and 0.0-1.4 V (AC//Mn_2O_3). EIS measurements were carried out in the frequency range 10 mHz – 1.0 MHz at open circuit potential with AC amplitude of 5 mV and the obtained data were fitted to an equivalent circuit model using NOVA 1.9 software.

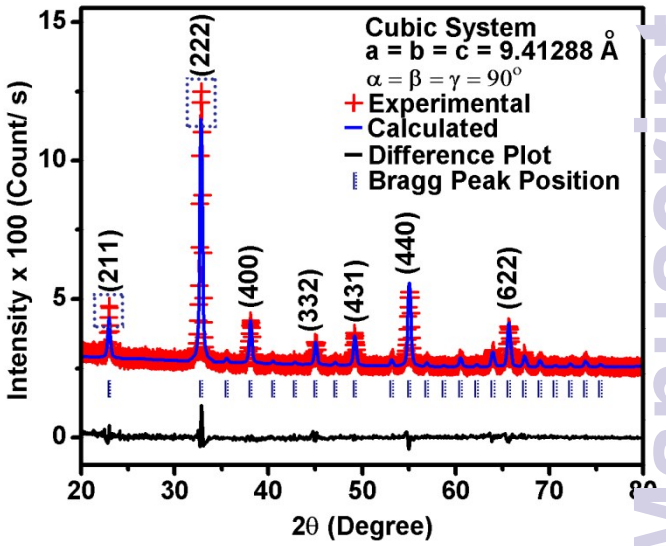

Fig.1 X-ray diffractogram of Mn-BTC MOF derived Mn_2O_3

Results and discussion

Structure, Morphology, and Thermal Stability of MOF derived nanostructured Mn_2O_3

Formation of Mn-BTC MOF has been checked by XRD. It is known that the crystallinity of Mn-BTC MOF is strongly influenced by the amount of solvent occluded in its pores.[49] The observed peaks in the X-ray diffractogram (shown in Fig.S1, ESI†) are very similar to those reported by Taylor et al.[50] and Zheng et al.[51] confirming successful synthesis of Mn-BTC MOF. TG analysis (Fig.S2, ESI†) showed that complete decomposition of Mn-BTC takes place at temperatures >480°C Accordingly, the as-synthesized Mn-BTC was calcined at 650°C to ensure complete conversion into Mn_2O_3. Fig.1 shows the X-ray diffractogram of Mn_2O_3, thus obtained. All of the observed diffraction peaks correspond to those of the cubic phase of Mn_2O_3 (space group Ia3) in agreement to JCPDS data file 00-041-1442. No additional peaks could be detected implying absence of possible impurity phases such as MnO or Mn_3O_4. Rietveld refinement of the phase produced a good fit with $R_{profile}$, (R_p), $R_{weightedprofile}$ (R_{wp}) and goodness of fit (χ^2) values of 15.650%, 21.949%, and 1.501%, respectively. The obtained lattice constant, a = 9.4128(8) Å, is also in good agreement

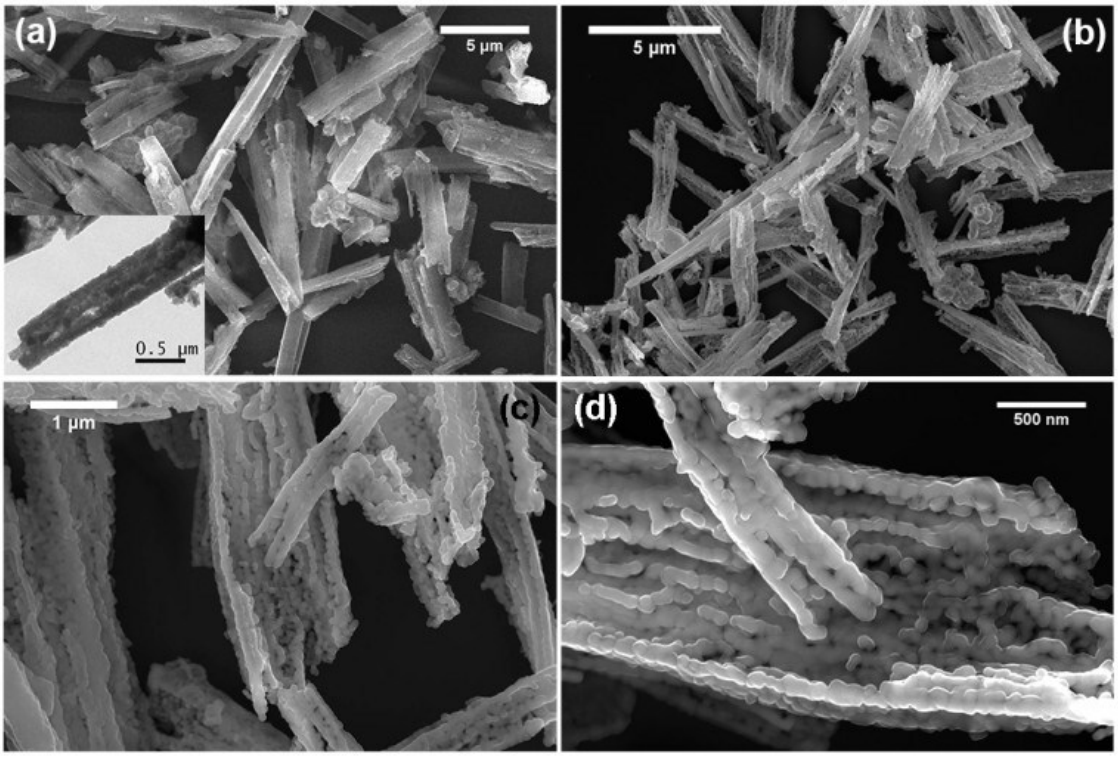

Fig.2 FESEM micrographs of Mn-BTC MOF (a) and the derived Mn_2O_3 (b-d) at various magnifications

with the literature values.[38] Hence, the XRD results indicate formation of Mn_2O_3 with high purity and crystallinity which is also corroborated by energy-dispersive X-ray spectroscopy (Fig.S3, ESI†). However, slight disparity has been observed between the calculated and experimentally observed peak intensities for (211) and (222) reflections suggesting preferred orientation of the Mn_2O_3 crystallites.

Morphology and microstructure of the parent Mn-BTC MOF and the derived Mn_2O_3 powders have been examined by FESEM and TEM. FESEM image, shown Fig.2a, reveals that the morphology of Mn-BTC consists of bar-shaped particles with corrugated edges. It is known that based on the starting precursor and solvent, different morphologies can result for Mn-BTC.[49,50] The morphology observed in the present study is similar to that reported in earlier work where Mn-BTC was synthesized by solvothermal route in alcoholic medium.[48,49,50] The dimension of the individual bars is found to be about 1 µm in width and between 2-20 µm in length. As can be seen from the low magnification FESEM image (Fig.2b), the general bar-shaped morphology of Mn-BTC seems to be retained after conversion into Mn_2O_3 through calcination. However, high magnification FESEM micrographs of Mn_2O_3 (Fig.2c & 2d) reveal that these bars are actually made of thin porous sheets stacked together where each of these sheets consists of an assembly of numerous spherical nanoparticles, organized like beaded chains. Formation of such kind of morphology could be originated from the presence of channelized pores in Mn-BTC which serve as escape paths for small molecules and gases produced by thermal decomposition and oxidation of the organic linkers during calcination. A closer look through TEM (Fig.3a-d) further discloses that these nanoparticles are not spherical, but are actually different shaped polyhedra, assembled in a linear pattern. Formation of differently shaped polyhedra can be explained on the basis of metal-ligand coordination in the metal organic framework. The metal center (Mn) is known to co-exist in various oxidation states ranging from +2 to +7. Therefore, different types of Mn-O coordinations exist in the synthesized Mn-BTC framework which upon calcination would lead to generation of different shaped and sized polyhedra of Mn_2O_3 as observed in the present case. This kind of arrangement would also create a large number of voids and spaces resulting in a substantially high surface area. The particles are faceted and well crystallized. Clear lattice fringes could be observed with a spacing of 0.39 nm that corresponds to (211) planes of Mn_2O_3 (Fig.3e). In the selected area diffraction (SAD) pattern (Fig.4f), observation of well-defined spots arranged in circular rings confirms the formation of well-crystallized polycrystalline Mn_2O_3 with characteristic planes clearly identified.

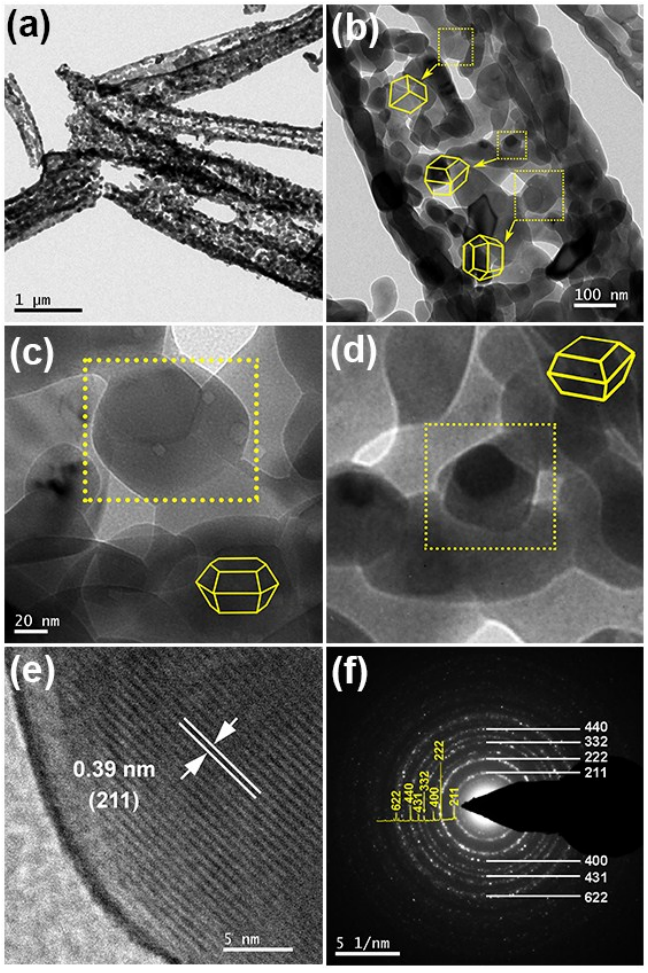

Fig.3 TEM images (a-d), HRTEM image (e) and selected area diffraction pattern (f) of MOF derived Mn_2O_3

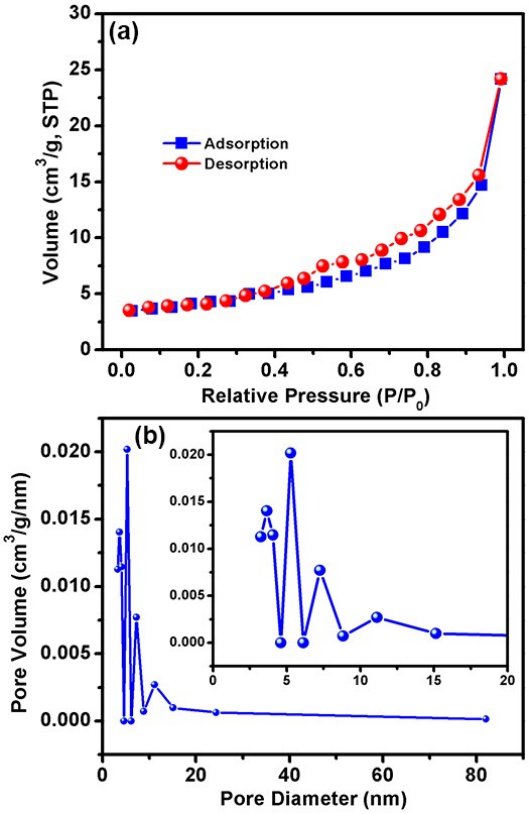

Fig.4 Adsorption desorption isotherms (a) and pore size distribution (b) of MOF derived Mn_2O_3

Surface area, pore size and their distributions are very significant parameters for the electrochemical performance of any electrode material whether it is applied for lithium-ion battery or supercapacitor. N_2 adsorption-desorption isotherms of synthesized Mn_2O_3 and corresponding pore size distributions are shown in Fig.4a-b. The isotherms are found to be convex in nature up to P/P_0 = 1.0, typical for type III isotherms. A small but wide hysteresis loop is observed in the range P/P_0 = 0.45-0.95 revealing a mixed H3 and H1 character with a mesoporous structure containing ink-bottle type of pores of size <4 nm.[52] The corresponding pore size distribution (Fig.4b), derived from the isotherms, also reveals mesoporous nature with a combination of narrow and broad size distributions at 4, 6, 7 and 12 nm. BET surface area of the synthesized Mn_2O_3 is found to be 44 m^2 g^{-1}. Observance of high surface area value can be attributed to the existence of a large number of voids and spaces, as observed in TEM (Fig.4). Such morphological features would be highly beneficial for easy access of electrolytes to the active sites and mass transport of Li^+ ions by diffusion.

Electrochemical characterization

Lithium-ion battery application

In order to identify the redox processes, cyclic voltammetry experiments have been conducted in two potential windows of 0.01-2.0 V and 0.01-3.0 V at a scan of 0.1 mV s^{-1}. The first four successive scans for each potential window are presented in Fig.5a (0.01-2.0 V) and Fig.5b (0.01-3.0 V). As expected, in both cases, the first cathodic scan shows similar features. A wide reduction peak positioned ~1.3 V indicates conversion of Mn^{3+} to Mn^{2+}.[38,53,54] A sharp cathodic peak observed at ~0.26 V can be assigned to the conversion of Mn^{2+} to Mn^0 along with formation of Li_2O, and also to the irreversible reactions of organic carbonates in the electrolyte with Li at this low potential forming an SEI layer.[55,56] A weak peak appearing at ~0.94 V may have originated from irreversible partial decomposition of the organic solvents. During the first anodic scan, within 0.01-2 V, only one moderately broad peak is observed at ~1.29 V (Fig.5a), representing oxidation of Mn^0 to Mn^{2+} and partial decomposition of Li_2O to Li. However, when the potential window is extended to 3 V, a second anodic peak appears at ~2.19 V due to further oxidation of Mn^{2+} to Mn^{3+} (Fig.5b). Interestingly, from the second cycle onward, significant difference in the redox processes, particularly in the cathodic peak due to $Mn^{2+} \rightarrow Mn^o$ is noticed depending on the potential window employed. In the 2 V window, the voltammograms consist of a single cathodic peak at ~0.51 V and the corresponding anodic peak at 1.29 V due to the reversible conversion reaction, $Mn^{2+} \leftrightarrow Mn^0$ (Fig.5a). Disappearance of the initial reduction peaks at 0.94 and

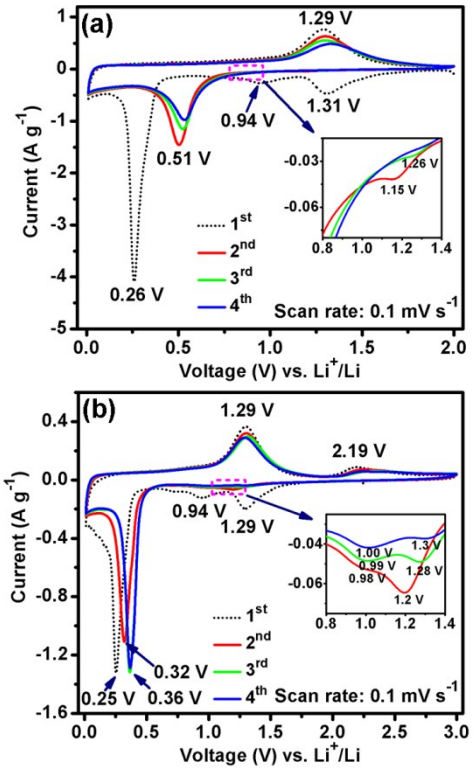

Fig.5 First four successive voltammetric scans of Mn_2O_3//Li cells in the potential windows of 0.01-2.0 V (a) and 0.01-3.0 V (b)

1.31 V corroborates absence of Mn^{3+} in the system. The observed shifting of the cathodic peak from 0.26 to 0.51 V is a common phenomenon for transition metal oxides originated from side reactions and structural rearrangements during the initial formation cycle.[57] In the 3 V window, two pair of redox couples are observed at 1.25/2.19 V ($Mn^{3+} \leftrightarrow Mn^{2+}$) and 0.36/1.29 V ($Mn^{2+} \leftrightarrow Mn^o$). These values are quite consistent with the previously reported values for redox peaks observed in 3 V window.[32,36,37] It is noticed that the shifting of the cathodic peak ($Mn^{2+} \rightarrow Mn^o$) with respect to the first scan is much lesser in the 3 V window than that observed in the 2 V window. This can be assigned to the field induced sluggish nature of the conversion of Mn^{3+} to Mn^{2+} as evidenced by the broad nature of the cathodic peak centered at ~1.27 V. The anodic and cathodic peak separation is a measure of the degree of the reversibility of a redox process. ($\Delta V_{Mn^{2+} \leftrightarrow Mn^o}$) is found to be 0.78 and 0.93 V for 2 V and 3 V window respectively. Thus, the cyclic voltammetry results indicate that the $Mn^{2+} \leftrightarrow Mn^o$ redox process would be more reversible when operated in the 2 V window. This is expected to lead to a better cycleability of the cell. Therefore, the electrochemical reactions for Mn_2O_3 in the potential window of 0.01-2.0 V can be expressed as below, based on a conversion mechanism:

(1)

(2)

(3)

Fig.6 shows a comparison of the galvanostatic discharge-charge profiles of Mn_2O_3 for the first cycle in both the potential windows (2 V and 3 V) at a constant current rate of C/8. The overall nature of the discharge-charge profiles is consistent with other transition-metal oxide anodes undergoing conversion based redox reactions. The first discharge profile is similar in both the potential windows: the potential drops from the open circuit potential (~2.4 V) to a voltage plateau at ~1.42 V, which can be linked to the

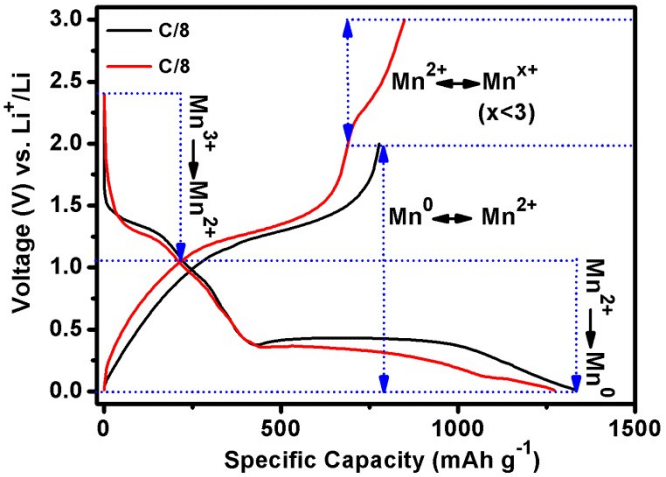

Fig.6 A comparison of the Galvanostatic discharge-charge profiles in the initial formation cycle of Mn_2O_3//Li cells in the potential windows of 0.01-2.0 V and 0.01-3.0 V

reduction of Mn_2O_3 to Mn_3O_4 (Equation 1). The potential then drops further to ~0.39 V with a new plateau which may have originated from the reduction of Mn_3O_4 to MnO (Equation 2). Thereafter, a long plateau is observed at ~0.36 V when the conversion reaction occurs with complete reduction of MnO to Mn and the formation of Li_2O (Equation 3). Finally, the potential drops down to the deep discharge limit of 0.01 V gradually forming the solid electrolyte interphase (SEI) layer. A high specific capacity of 1140 mAh g^{-1}, about 12% higher than the theoretical value (1018 mAh g^{-1}) is observed in the first discharge cycle. The surplus capacity could possibly be linked to the decomposition of the electrolyte at low potential producing a SEI layer and extra lithium storage at the metal/Li_2O interface.[58-62] The first charge profiles are also similar up to 2 V for both the potential windows with appearance of a sloppy voltage plateau between 1.0-1.5 V, which can be related to the oxidation of Mn(0) to form MnO. However, an additional voltage plateau between 2.0-2.5 V is observed in the 3 V window indicating further oxidation of MnO. The initial charge capacities are found to be 778 and 890 mAh g^{-1} in the 2 V and 3 V window respectively. The obtained capacity in the 3 V window of the present MOF derived Mn_2O_3

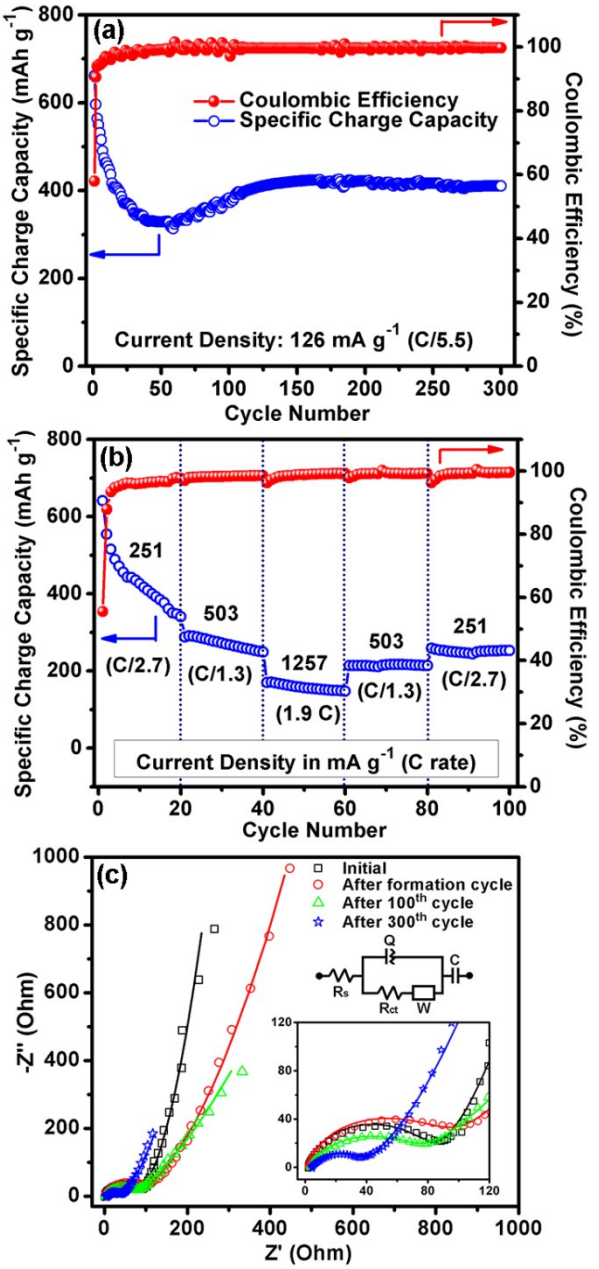

Fig.7 Electrochemical properties of Mn_2O_3//Li cells in the potential window of 0.01-2.0 V: cycling test (a) rate performance (b) and impedance spectra (c)

is superior to the values reported for Mn_2O_3 nanostructures synthesized by wet chemical routes.[23,27,33] While the 2 V capacity for Mn_2O_3 has not been reported previously, the observed capacity of 778 mAh g^{-1} is much higher than other 2 V metal oxide anodes, such as TiO_2.[63]

Fig.7a shows the cyclic performance carried out at 126 mA g^{-1} (C/5.5) in the potential window of 0.01-2.0 V. It is observed that initially for about 40 cycles there is a sharp decrease in capacity followed by a gradual increase till about 120 cycles. Thereafter, a capacity of ~410 mAh g^{-1} is observed till 300 cycles. Such behavior is common for transition metal oxide anodes. Initially, during the conversion reaction, a solid SEI

layer is formed that resists the delithiation process. Characterization of the electrodes after 5 and 10 cycles have been carried out to estimate the degradation. Fig.S4, ESI† shows the PXRD patterns obtained from the electrode after 5 and 10 cycles in the charged state (2.0 V). It is found that the intensity for the Li_2CO_3 phase (originating from the reaction of Li with electrolyte at lower potentials) increases with cycling indicating a thicker SEI layer. This might explain the observed initial decrease in capacity. FESEM image of the electrode after 10 cycles (Fig.S5, ESI†) shows partial breakage of the nanobars into smaller particles. Upon continued cycling, a polymeric gel is known to form gradually during cycling which may act as Li^+ insertion/de-insertion sites. The steady increase in capacity may also arise from the surface storage by the orderly organization of residual metallic Mn.[0,64,65] Except for the few initial cycles, the coulombic efficiency approaches 100% demonstrating good reversibility of the cell. Also, no noticeable change in the GCD profiles has been observed upon prolonged cycling (Fig.S6, ESI†). Rate performance studies have been carried out by cycling the cell between 0.05-2.0 V at different current densities of 251 (C/2.7), 503 (C/1.3) and 1257 mA g^{-1} (1.9C) for 20 cycles at each rate continuously and the results are presented in Fig.7b. It is observed that at comparatively lower current densities of 251 (C/2.7) and 503 mA g^{-1} (C/1.3), a steady decrease in capacity occurs. This can be assigned to the general declining trend up to ~40 cycles as observed in Fig.7a during cycling test. But between 40 and 60 cycles, even at a high current density of 1257 mA g^{-1} (1.9C), no significant capacity fading is observed with an average value of ~150 mAh g^{-1}. Again, to test the capacity restoration ability, the cell has been cycled again at 503 (C/1.3) and 251 mA g^{-1} (C/2.7) for 20 cycles each and capacity values of 214 and 254 mAh g^{-1} have been obtained with no apparent fading. The ability to withstand high charge discharge rate and prolonged cycle life can be attributed to the unique porous structure of this MOF derived Mn_2O_3. Fig.7c shows the Nyquist plots recorded at different cycling stage in the frequency range of 100 kHz to 1 mHz with an equivalent circuit model in the inset. The shapes of the plots comprise of one semicircle at the high to intermediate frequency region (corresponds to the L-C part), followed by a linear component at the low frequency region (Warburg and capacitive part). Analyses of impedance spectra shows that the as-assembled cell has a low solution resistance (R_s) of 2.2 Ω which increases marginally with cycling

Table.1 Fitted parameters obtained from impedance spectra of Mn_2O_3//Li Cells at different cycling interval

Cycle Number	Rs (Ohm)	Rct (Ohm)	Q/CPE		W (mMho)	C (mF)
			Y_0 (μMho)	N		
As assembled	2.2	76.9	6.7	0.92	4.06	1.3
1	2.2	86.6	7.7	0.90	1.93	1.5
100	3.1	71.1	27.1	0.76	3.81	11.7
300	4.2	33.4	84.8	0.71	10.7	16.1

and reaches to only 4.2 Ω after 300 cycles. This demonstrates the stability of the Mn_2O_3 electrode where the commonly observed phenomenon of Mn dissolution into the electrolyte is suppressed. Initially, the charge transfer resistance (R_{ct}) increases from 76.9 Ω to 86.6 Ω after the formation cycle. With continued cycling, R_{ct} is found to decrease indicating gradual increase in inter-grain charge transfer rate. This also explains the observed high rate performance (Fig.7b) and steady cycling behavior between 100-300 cycles (Fig7a).

Electrochemical supercapacitor application

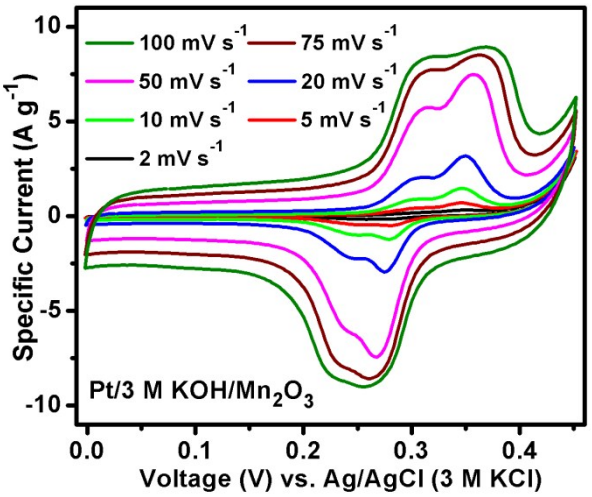

Fig.8 Cyclic voltammograms of Mn_2O_3 supercapacitor electrode at various scan rates of 2-100 mVs^{-1} in three-electrode configuration

In addition to a 2 V LIB anode, the potential of using MOF derived Mn_2O_3 as electrochemical supercapacitor is also examined both in three-electrode configuration and in two-electrode asymmetric configuration. The capacitive properties are first studied by cyclic voltammetry in three electrode configuration using Pt as counter electrode and Ag/AgCl as reference electrode in 3 M KOH as electrolyte. The voltammograms, obtained by measuring the current responses for potential sweep in the range 0.0-0.45 V at different rates ranging from 2 mVs^{-1} to 100 mVs^{-1}, are shown in Fig.8. The overall shape of the voltammograms is quasi-rectangular with a couple of broad oxidation peaks centered at ~0.30 and ~0.35 V and reduction peaks centered at ~0.24 and ~0.27 V are observed indicating that the capacitive behavior of Mn_2O_3 comprises of a prominent pseudocapacitive part (faradic) along with the electric double layer capacitance (EDLC; non-faradic). While the origin of EDLC can be related to the adsorption of electrolyte cations (K^+ in the present case) on the surface of Mn_2O_3, pseudocapacitnace arises from electron transfer at the Mn sites ($Mn^{3+} \leftrightarrow Mn^{4+}$) during which the charge balance is maintained by reversible insertion/extraction of OH^- from the electrolyte.[45] The well crystallized faceted structure of the MOF derived Mn_2O_3 facilitates the adsorption

and subsequent intercalation of OH^- into the cubic lattice. Recently, Lin et al.[66] have shown that in mixed valence manganese oxide supercapacitor (Mn_2O_3 and Mn_3O_4 mixture), the charge transfer occurs through conversion of lower valence states of $Mn^{2.67+}$ (Mn_3O_4) and Mn^{3+} (Mn_2O_3) into higher valence Mn^{4+}. Due to the dominant pseudocapactive component, the observed CV profiles of Mn_2O_3 electrode versus Ag/AgCl (3.0 M KCl) are not perfectly rectangular. From the observations of CV, the following electrochemical reactions can be proposed to account for the pseudocapacitance of Mn_2O_3:

(4)

For pseudocapacitors, the peak current in CV is not constant across the entire potential range. Therefore, galvanostatic charge-discharge (GCD) measurements were used to calculate the specific capacitance by the following equation:

(5)

where, is the specific capacitance in three-electrode configuration, is the discharge current, is the discharge time, is the potential change during the discharge excluding IR drop and is the mass of the electrode. As shown in Fig.9a-b, GCD profiles at different current densities (0.2-30 A g^{-1}) are quasi-triangular in nature showing typical pseudocapacitive behavior corroborating the observations in CV. No change in the nature of the profiles is observed with increase in current density up to as high as 30 A g^{-1}. C_s values

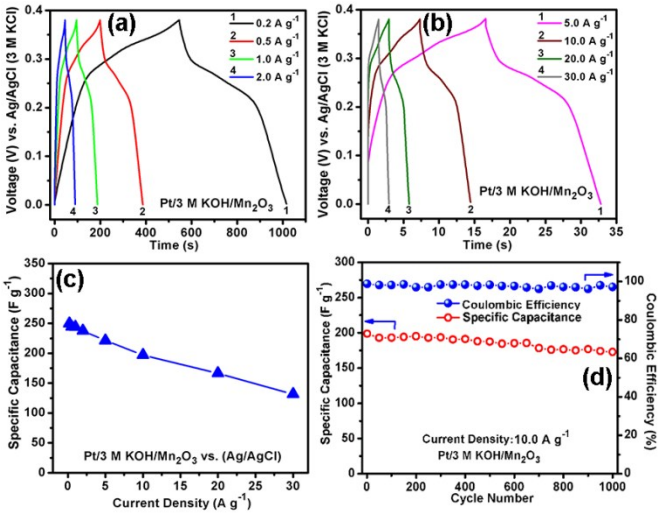

Fig.9 Electrochemical properties of Mn_2O_3 as supercapacitor in the potential window of 0.0-0.37 V in three-electrode configuration: Galvanostatic charge-discharge profiles at various current densities of 0.2-30.0 A g^{-1} (a, b) variation of specific capacitance with increasing current density (c) and cycling performance and coulombic efficiency (d)

of 249.7, 244.5, 244, 237.7, 221, 197, 166.4 and 131.5 F g^{-1} have been found at current densities of 0.2, 0.5, 1, 2, 5, 10, 20 and 30 A g^{-1} respectively (Fig.9c). These values are superior to the values reported in the literature for Mn_2O_3 in the pristine form synthesized by wet-chemical route,[35,40,47] and can be assigned to the mesoporous nature of the MOF derived Mn_2O_3 providing easy access of the electrolyte to the interior surfaces. The decrease in Cs with increasing current density indicates that the redox processes are diffusion limited. In order to check the cycleability, the cell was subjected to 1000

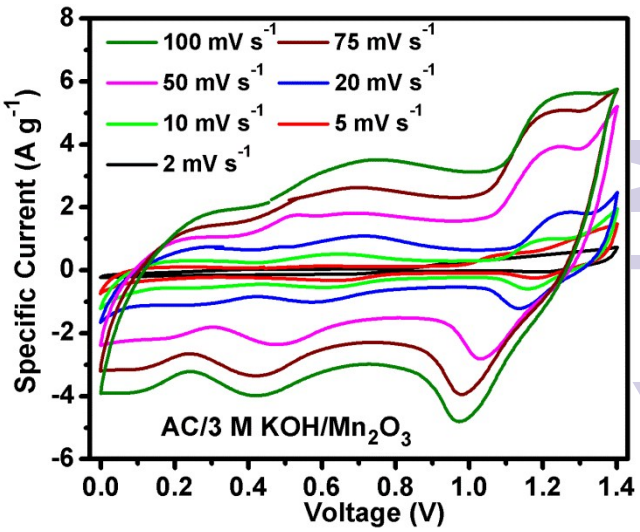

Fig.10 Cyclic voltammograms of AC//Mn_2O_3 asymmetric supercapacitor cells at various scan rates of 2-100 mV s^{-1}

continuous charge-discharge cycles at a high current density of 10 A g^{-1} whereby retention of ~88% of capacitance is observed (Fig.9d). In further investigation, to mimic the physical configuration of practical cells, two-electrode asymmetric supercapacitor pouch cells were constructed with the MOF derived Mn_2O_3 as the positive electrode and commercial activated carbon (AC) as the negative electrode. Since activated carbon is known to exhibit EDLC behavior, at first, cyclic voltammetry of the AC has been carried out against Pt as counter electrode and Ag/AgCl as reference electrode in the potential window of -1.0 to 0.0 V (Fig.S7, ESI†). A capacitance value of ~ 80 F g^{-1} is observed at a scan rate of 2 mV s^{-1} which is comparable to the values reported earlier for AC.[67] Fig.10 shows the cyclic voltammograms for the AC//Mn_2O_3 asymmetric cells at various scan rates ranging from 2 to 100 mVs^{-1}. Notably, the potential window of the cell could be extended up to 1.5 V by combining Mn_2O_3 with AC. Thus, the energy density could be substantially increased. Similar extension of potential window has been reported in earlier studies with symmetric Ru//Ru cells (1.8 V),[68] and RuO_2//RuO_2 cell (1.6 V) in aqueous electrolytes. The observed voltammograms (Fig.10) are quasi-rectangular indicating dual existence of EDLC and pseudocapacitance. The GCD profiles of these asymmetric cells are shown in Fig.11a (for current densities of 0.2-2.0 A g^{-1}) and in Fig.S8, ESI† (for current

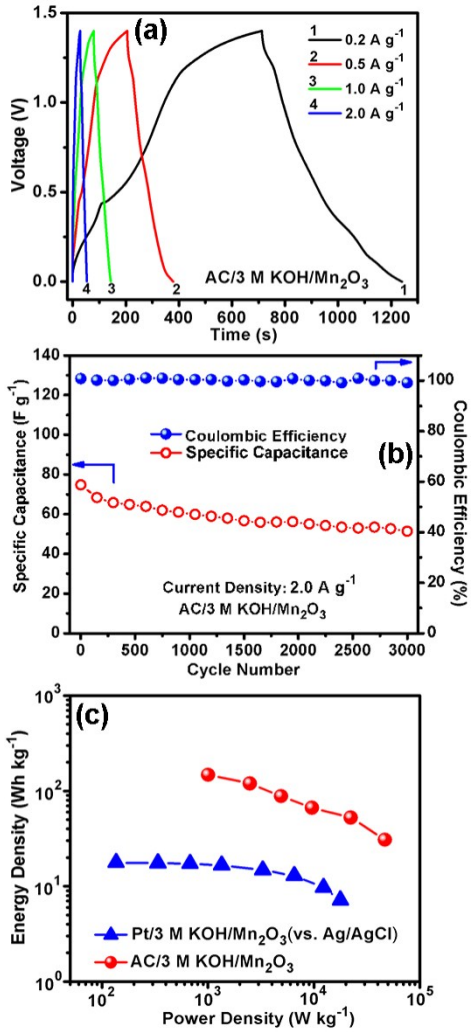

Fig.11 Electrochemical properties of AC//Mn_2O_3 asymmetric supercapacitor cells in the potential window of 0.0-1.4 V: Galvanostatic charge-discharge profiles at various current densities of 0.2-2.0 A g^{-1} (a) cycling performance along with coulombic efficiency (b) and Ragone plot in comparison with Pt//Mn_2O_3 cells (c)

densities of 5 and 10 A g^{-1}). The specific capacities have been calculated using the following equation:[69]

(6)

Where, is the specific capacitance, is the discharge current, is the discharge time, is the potential change during the discharge excluding IR drop and m' is the average mass of Mn_2O_3 and AC electrodes. It is known that the specific capacity values of two-electrode cells are always much lower

than those obtained from single electrodes in three-electrode configuration.[70] A high specific capacity (C_S) of ~150 F g^{-1} could be found at a current density of 0.2 A g^{-1}. Cycling test conducted at a relatively higher current density of 2 A g^{-1} shows ~75% retention of capacity after 3000 continuous charge discharge cycles (Fig.11b).

Based on the GCD measurements at different current densities, the energy density (E) and power densities (P) have been calculated using the following equations:

(7)

(8)

Where, C is the specific capacitance obtained at respective current density. Supercapacitors are expected to deliver a reasonable energy density at a high power density. Fig.11c shows the Ragone plots (energy density vs. power density) for both AC//Mn_2O_3 and Pt//Mn_2O_3 cells. Enhancement of nearly an order of magnitude in the energy density is observed for the AC//Mn_2O_3 asymmetric cell compared to Pt//Mn_2O_3 cell at all power densities. The Pt//Mn_2O_3 cell gives an energy density of 17.7 Wh kg^{-1} at a low power density of 136 W kg^{-1}. In contrast, the AC//Mn_2O_3 cell delivers an energy density of 147.4 Wh kg^{-1} at a power density of 1004 W kg-1. Even at a very high power density of 46831 W kg^{-1}, the cell still delivers an energy density of 30.7 Wh kg^{-1}. While there is no prior report on AC//Mn_2O_3 asymmetric cells, the observed energy densities are much higher than observed for AC//MnO_2,[71] AC//RuO_2,[72] AC//AC,[73] or even RuO_2//RuO_2 (18.77 Wh kg^{-1} at a power density of 500 W kg^{-1}).[74]

Conclusions

In conclusion, we have demonstrated an easy and scalable route for synthesizing mesoporous Mn_2O_3 nanobars comprising of a unique beaded-chain particle morphology derived from Mn-BTC MOF. The synthesized Mn_2O_3 can be used as a Li-ion battery anode in the 2 V window with a relatively high capacity of ~410 mAh g^{-1} at 126 mA g^{-1} (C/5.5) as well as for supercapacitors with an ultrahigh energy density of 147.4 Wh kg^{-1} at a power density of 1004 W kg^{-1}. The present work would further stimulate the ongoing search for high performance materials with pre-designed nanoarchitecture for energy storage.

Acknowledgements

The authors thank Director, CSIR-CGCRI for kind permission to publish this work. Financial support from CSIR via TAPSUN NWP0056 project is gratefully acknowledged. S Maiti thanks CSIR India for a senior research fellowship.

References

1 P. Poizot, S. Laruelle, S. Grugeon, L. Dupont and J. M. Tarascon, *Nature*, 2000, **407**, 496-499.
2 H. Li, Z. Wang, L. Chen and X. Huang, *Adv. Mater.*, 2009, **21,** 4593-4607.
3 Z. Y. Wang, L. Zhou and X. W. Lou, *Adv. Mater.*, 2012, **24,** 1903-1911.
4 B. Wang, J. S. Chen, H. B. Wu, Z. Y. Wang and X. W. Lou, *J. Am. Chem. Soc.*, 2011, **133**, 17146-17148.
5 X. W. Li, S. L. Xiong, J. F. Li, X. Liang, J. Z. Wang, J. Bai and Y. T. Qian, *Chem. Eur. J.*, 2013, **19**, 11310-11319.
6 H. B. Wu, J. S. Chen, H. H. Hng and X. W. Lou, *Nanoscale*, 2012, **4**, 2526-2542.
7 L. L. Zhang and X. S. Zhao, *Chem. Soc. Rev.*, 2009, **38**, 2520-2531.
8 Y. Shao, M. F. El-Kady, L. J. Wang, Q. Zhang, Y. Li, H. Wang, M. F. Mousavi and R. B. Kaner, *Chem. Soc. Rev.*, 2015, **44**, 3639-3665.
9 M. C. Orilall and U. Wiesner, *Chem. Soc. Rev.*, 2011, **40**, 520-535.
10 J. Duay, E. Gillette, J. Hu and S. B. Lee*, Phys. Chem. Chem. Phys.*, 2013, **15**, 7976-7993.
11 J. Deng, H. Ji, C. Yan, J. Zhang, W. Si, S. Baunack, S. Oswald, Y. Mei and O. G. Schmidt, *Angew. Chem. Int. Ed.*, 2013, **52**, 2326-2330.
12 C. Yan, W. Xi, W. Si, J. Deng and O. G. Schmidt, *Adv. Mater.,* 2013, **25**, 539-544.
13 L. Zhang, J. Deng, L. Liu, W. Si, S. Oswald, L. Xi, M. Kundu, G. Ma, T. Gemming, S. Baunack, F. Ding, C. Yan and O. G. Schmidt, *Adv. Mater.,* 2014, **26**, 4527-4532.
14 Q. Zhang, E. Uchaker, S. L. Candelaria and G. Cao, *Chem. Soc. Rev.*, 2013, **42**, 3127-3171.
15 W. Xia, A. Mahmood, R. Zou and Q. Xu, *Energy Environ. Sci.*, 2015, **8**, 1837-1866.
16 L. Hu and Q. Chen, *Nanoscale*, 2014, **6**, 1236-1257.
17 C. Sun, J. Yang, X. Rui, W. Zhang, Q. Yan, P. Chen, F. Huo, W. Huang and X. Dong, *J. Mater. Chem.* A, 2015, **3**, 8483-8488.
18 K. J. Lee, T.-H. Kim, T. K. Kim, J. H. Lee, H.-K. Song and H. R. Moon, *J. Mater. Chem. A*, 2014, **2**, 14393-14400.
19 G. Huang, F. Zhang, L. Zhang, X. Du, J. Wang and L. Wang, *J. Mater. Chem. A*, 2014, **2**, 8048-8053.
20 Y. C. Qiu, G. L. Xu, K. Y. Yan, H. Sun, J. W. Xiao, S. H. Yang, S. G. Sun, L. M. Jin and H. Deng, *J. Mater. Chem.*, 2011, **21**, 6346-6353.
21 X. D. Xu, R. G. Cao, S. Jeong and J. Cho, *Nano Lett.*, 2012, **12**, 4988-4991.
22 Y. Chen, H. Xia, L. Lu and J. M. Xue, *J. Mater. Chem.*, 2012, **22**, 5006-5012.
23 L. L. Wang, H. X. Gong, C. H. Wang, D. K. Wang, K. B. Tang and Y. T. Qian, *Nanoscale*, 2012, **4**, 6850-6855.
24 Y. Deng, Z. Li, Z. Shi, Hui Xu, F. Peng and G. Chen, *RSC Advances*, 2012, **2**, 4645-4647.
25 Y. Dai, H. Jiang, Y. Hu and C. Li, *RSC Adv.*, 2013, **3**, 19778-19781.
26 Y. Zhang, Y. Yan, X. Wang, G. Li, D. Deng, L. Jiang, C. Shu and C. Wang, *Chem. Eur. J.*, 2014, **20**, 6126-6130.
27 H. B. Lin, H. B. Rong, W. Z. Huang, Y. H. Liao, L. D. Xing, M. Q. Xu, X. P. Li and W. S. Li, *J. Mater. Chem.* A, 2014, **2**, 14189-14194.
28 M.-W. Xu, Y.-B. Niu, S.-J. Bao and C. M. Li, *J. Mater. Chem. A*, 2014, **2**, 3749-3755.
29 L. Chang, L. Mai, X. Xu, Q. An, Y. Zhao, D. Wang and X. Feng, *RSC Adv.*, 2013, **3**, 1947-1952.
30 B. C. Sekhar, G. Babu and N. Kalaiselvi, *RSC Adv.*, 2015, **5**, 4568-4577.
31 X. Zhang, Y. Qian, Y. Zhu and K. Tanga, *Nanoscale*, 2014, **6**, 1725-1731.
32 Z. Bai, Y. Zhang, Y. Zhang, C. Guo, B. Tang and D. Sun, *J. Mater. Chem. A*, 2015, **3**, 5266-5269.
33 R. Liu, S. Zhao, M. Zhang, F. Feng and Q. Shen, *Chem. Commun.*, 2015, **51**, 5728-5731.
34 Y. Cai, S. Liu, X. M. Yin, Q. Y. Hao, M. Zhang and T. H. Wang, *Physica E*, 2010, **43**, 70-75.
35 S. L. Chen, F. Liu, Q. J. Xiang, X. H. Feng and G. H. Qiu, *Electrochim.. Acta*, 2013, **106**, 360-371.
36 Y. Qiu, G.-L. Xu, K. Yan, H. Sun, J. Xiao, S. Yang, S.-G. Sun, L. Jind and H. Deng, *J. Mater. Chem.*, 2011, **21**, 6346-6353.
37 H. W. Shim, A. H. Lim, K. M. Min and D. W. Kim, *CrystEngComm*, 2011, **13**, 6747-6752.
38 P. Pal, A. K. Giri, S. Mahanty and A. B. Panda, *CrystEngComm*, 2014, **16**, 10560-10568.
39 Q. Li, L. Yin, Z. Li, X. Wang, Y. Qi and J. Ma, *ACS Appl. Mater. Interfaces*, 2013, **5**, 10975-10984.
40 T. Nathan, M. Cloke and S. R. S. Prabaharan, *J. Nanomater.* 2008, **2008**, Article ID 948183.
41 X. Wang, L. Liu, X. Wang, L. Yi, C. Hu and X. Zhang, *Mat. Sci. Eng. B,* 2011, **176**, 1232-1238.
42 S. Chen, F. Liu, Q. Xiang, X. Feng and G. Qiu, *Electrochim. Acta*, 2013, **106**, 360-371.
43 S. H. Lee, H. Lee, M. S. Cho, J.-D. Nam and Y. Lee, *J. Mater. Chem. A*, 2013, **1**, 14606-14611.
44 Y. Zhang, M. Ma, J. Yang, W. Huang and X. Dong, *RSC Adv.*, 2014, **4**, 8466-8471.
45 A. T. Chidembo, S. H. Aboutalebi, K. Konstantinov, C. J. Jafta, H. K. Liu and K. I. Ozoemena, *RSC Adv.*, 2014, **4**, 886-892.
46 K.-W. Park, *J. Mater. Chem. A*, 2014, **2**, 4292-4298.
47 W. Li, J. Shao, Q. Liu, X. Liu, X. Zhou and J. Hu, *Electrochim. Acta*, 2015, **157**, 108-114.
48 S. Maiti, A. Pramanik, U. Manju and S. Mahanty, *ACS Appl. Mater. Interfaces*, 2015, **7**, 16357-16363.
49 H. Reinsch and N. Stock, *CrystEngComm*, 2013, **15**, 544-550
50 K. M. L. Taylor, W. J. Rieter and W. Lin, *J. Am. Chem. Soc.*, 2008, **130**, 14358-14359.
51 F. Zheng, G. Xia, Y. Yang and Q. Chen, *Nanoscale*, 2015, **7**, 9637-9645.
52 Z. Qin, B. Shen, X. Gao, F. Lin, B. Wang and C. Xu, *J. Catal.* 2011, **278**, 266-275.
53 Y. Zhang, Y. Yan, X. Wang, G. Li, D. Deng, L. Jiang, C. Shu and C. Wang, *Chem. Eur. J.*, 2014, **20**, 1-6.
54 Y. Deng, Z. Li, Z. Shi, H. Xu, F. Peng and G. Chen, *RSC Adv.*, 2012, **2**, 4645-4647.
55 L. F. Xiao, Y. Y. Yang, J. Yin, Q. Li and L. Z. Zhang, *J. Power Sources*, 2009, **194**, 1089-1093.
56 Y. Ren, A. R. Armsrong, F. Jiao and P. G. Bruce, *J. Am. Chem. Soc.*, 2010, **132**, 996-1004.
57 C. Yuan, H. B. Wu, Y. Xie and X. W. Lou, *Angew Chem Int. Ed.*, 2014, **53**, 1488-1504.
58 Y. C. Qiu, G. L. Xu, K. Y. Yan, H. Sun, J. W. Xiao, S. H. Yang, S. G. Sun, L. M. Jin and H. Deng, *J. Mater. Chem.*, 2011, **21**, 6346 -6353.
59 X. F. Fang, X. Lu, X. W. Guo, Y. Mao, Y. S. Hu, J. Z. Wang, Z. X. Wang, F. Wu, H. K. Liu and L. Q. Chen, *Electrochem. Commun.*, 2010, **12**, 1520-1523.
60 S. Nayak, S. Malik, S. Indris, J. Reedijk and A. K. Powell, *Chem. Eur. J.*, 2010, **16**, 1158-1162.
61 F. L. Wang, J. R. Liu, J. Kong, Z. J. Zhang, X. Z. Wang, M. Itoh, K. I. Machida, *J. Mater. Chem.*, 2011, **21**, 4314-4320.
62 Y. Cai, S. Liu, X. M. Yin, Q. Y. Hao, M. Zhang and T. H. Wang, *Physica E*, 2010, **43**, 70-75.
63 P. Cui, B. Xie, X. Li, M. Li, Y. Li, Y. Wang, Z. Liu, X. Liu, J. Huang, D. Song and J. M. Mbengue, *CrystEngComm*, 2015, DOI: 10.1039/C5CE01600B
64 L. Chang, L. Mai, X. Xu, Q. An, Y. Zhao, D. Wang and X. Feng, *RSC Adv.*, 2013, **3**, 1947-1952.

65 R. Liu, S. Zhao, M. Zhang, F. Feng and Q. Shen, *Chem. Commun.,* 2015, **51**, 5728-5731.
66 C.-K. Lin, K.-H. Chuang, C.-Y. Lin, C.-Y. Tsay, and C.-Y. Chen, *Surf. Coat. Tech.*, 2007, **202**, 1272-1276.
67 D. Saha, Y. Li, Z. Bi, J. Chen, J. K. Keum, D. K. Hensley, H. A. Grappe, H. M. Meyer, S. Dai, M. P. Paranthaman and A. K. Naskar, *Langmuir*, 2014, **30**, 900-910.
68 H. Xia, B. Li and L. Lu, *RSC Adv.*, 2014, **4**, 11111-11114.
69 S. Maiti, A. Pramanik, and S. Mahanty, *ACS Appl. Mater. Interfaces*, 2014, **6**, 10754-10762.
70 J. Yan, Z. Fan, W. Sun, G. Ning, T. Wei, Q. Zhang, R. Zhang, L. Zhi, and F. Wei, *Adv. Funct. Mater.*, 2012, **22**, 2632-2641.
71 H. Jiang, C. Li, T. Sun and J. Ma, *Nanoscale*, 2012, **4**, 807-812.
72 A. L. M. Reddy and S. Ramaprabhu, *J. Phys. Chem. C*, 2007, **111**, 7727-7734.
73 Z. Lei, N. Christov, L. L. Zhang and X. S. Zhao, *J. Mater. Chem.*, 2011, **21**, 2274-2281.
74 H. Xia, Y. S. Meng, G. Yuan, C. Cui and L. Lu, *Electrochem sol St Lett*, 2012, **15**, A60-A63.

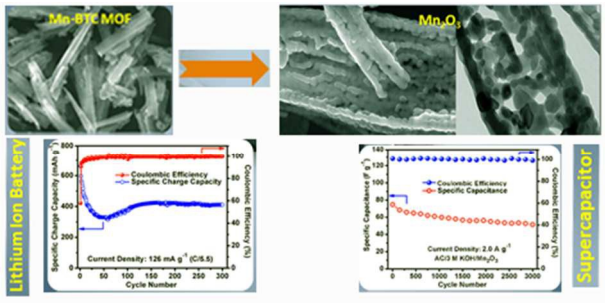

MOF-derived Mn_2O_3 shows high capacity of ~410 $mAhg^{-1}$ as 2 V anode and an ultrahigh energy density of 147.4 $Whkg^{-1}$ as supercapacitor.